RESEARCH ARTICLE | MARCH 03 2026

A versatile two-dimensional terahertz spectroscopy platform with dual independently controlled intense pulses

X. B. Wang ; L. Y. Shi ; S. J. Zhang ; J. Y. Yuan ; Y. T. Li ; J. L. Luo ; T. Dong ; N. L. Wang

Rev. Sci. Instrum. 97, 033001 (2026)
https://doi.org/10.1063/5.0281877

Review of Scientific Instruments ARTICLE pubs.aip.org/aip/rsi

A versatile two-dimensional terahertz spectroscopy platform with dual independently controlled intense pulses

Cite as: Rev. Sci. Instrum. 97, 033001 (2026); doi: 10.1063/5.0281877
Submitted: 22 May 2025 • Accepted: 12 February 2026 •
Published Online: 3 March 2026

X. B. Wang,[1,a] L. Y. Shi,[2] S. J. Zhang,[1] J. Y. Yuan,[2] Y. T. Li,[1] J. L. Luo,[1] T. Dong,[2,3,a] and N. L. Wang[2,3,a]

AFFILIATIONS

[1] Beijing National Laboratory for Condensed Matter Physics, Institute of Physics, Chinese Academy of Sciences, Beijing 100190, China
[2] International Center for Quantum Materials, School of Physics, Peking University, Beijing 100871, China
[3] Tsung-Dao Lee Institute, Department of Physics and Astronomy, Shanghai Jiao Tong University, Shanghai 200240, China

[a] **Authors to whom correspondence should be addressed:** xinbowang@iphy.ac.cn, taodong@pku.edu.cn, and nlwang@pku.edu.cn

ABSTRACT

We present a two-dimensional terahertz (2D THz) spectroscopy platform employing dual high-intensity THz sources generated in separate $LiNbO_3$ crystals via the tilted-pulse-front technique. An integrated periscope beam combiner enables efficient combination of the two THz beams and precise overlap at both the sample and detection positions. The platform provides independent control over the polarization, spectrum, and intensity of each THz pulse, thereby increasing experimental flexibility. To demonstrate the instrument's performance, we investigate nonlinear wave-mixing in silicon under dual-frequency excitation. Polarization-dependent nonlinear signals up to the 11th order in a 2D spectrum were resolved at room temperature using this tabletop laser system. These results underscore the capability of the instrument to explore complex material responses at THz frequencies and elucidate underlying nonlinear mechanisms.

I. INTRODUCTION

Multidimensional spectroscopy, pioneered in nuclear magnetic resonance (NMR),[1] has evolved into a powerful technique for unraveling the intricate dynamics and interactions within complex systems.[2] Its applications have been extended to diverse spectral regions, including infrared, optical, and microwave frequencies,[3–10] providing insights into vibrational relaxation, energy transfer, and inter-molecular couplings. These experiments rely on precisely controlled sequences of pulses to induce high-order nonlinear responses, revealing correlations and energy flows that are inaccessible to linear spectroscopy.

Despite its proven capabilities, implementing multidimensional spectroscopy in the THz frequency range presents formidable experimental challenges. A key obstacle is the generation of THz pulses with sufficient electric field strength to elicit measurable nonlinear signals from the low-energy excitations in quantum materials, such as phonons, magnons, and other collective modes. In recent years, the rapid advancement of high-field THz technologies has significantly propelled the field forward.[11,12] While free-electron lasers provide intense THz radiation,[13] modern tabletop laser-based THz sources have achieved electric field strengths up to MV/cm,[14–21] enabling the application of nonlinear THz spectroscopy techniques.[22–31]

Among the nonlinear THz techniques, 2D THz spectroscopy has rapidly developed in recent years and is applied to different areas. It captures the time-resolved nonlinear response from dual intense THz pulses, enabling exploration of coupling between different collective modes through the cross peaks in the 2D spectrum.[32–45] This capability provides unprecedented insight into the microscopic origins of cooperative phenomena in quantum materials, such as superconductivity,[46–52] charge density waves,[53] and topological states.[54,55] In addition, 2D THz spectroscopy enables the identification of the intrinsic broadening mechanisms by

measuring the lineshapes of the corresponding excitation spectrum.[48,56] Moreover, it has exhibited considerable potential for the investigation of ultrafast processes occurring on femtosecond to picosecond timescales, rendering it indispensable for the study of transient states and the coherent control of materials under non-equilibrium conditions.[26,30,57]

Two-dimensional terahertz spectroscopy provides a unique and powerful insight into ultrafast dynamics, but its widespread application is limited by instrumental challenges. A primary challenge is generating and independently controlling two high-intensity THz beams,[26,30,57] including their polarization, spectrum, and intensity. Precise control over these parameters is required to isolate specific interaction pathways and coupling mechanisms.[58] Existing experimental setups often involve a trade-off between versatility and efficiency. For example, a single-crystal generation setup avoids alignment complexities but lacks the versatility for polarization-dependent studies, which are crucial for probing material anisotropies.[59] Conversely, dual-source platforms often use a 45° wire-grid polarizer as a beam combiner, which results in an electric field loss of over 30% in at least one of the beams.[56] The combination of reduced field strength and alignment complexity in dual-beam configurations limits the ability to drive and probe extreme nonlinear responses, representing a major bottleneck for the advancement of the 2D THz technique.

In this work, we have designed and constructed a novel 2D THz spectroscopy platform that achieves both high efficiency and complete experimental flexibility. Our approach combines two independent high-field THz sources with a custom periscope wire-grid combiner, which preserves nearly the entire electric field from each source. Furthermore, the periscope's dual-mirror design provides two independent degrees of freedom for alignment, which enables robust and precise spatial overlap and overcomes the alignment challenge in 2D THz spectroscopy. Our system offers complete independent control over the polarization, spectral content, and intensity of each beam, allowing experimental configurations not feasible in previous table-top 2D THz systems. To demonstrate these capabilities, we performed a dual-frequency excitation experiment on silicon. The resulting 2D THz spectra reveal nonlinear wave-mixing signals up to the 11th order at room temperature. To our knowledge, this is the first room-temperature 2D demonstration of such high-order responses in a compact system. Our work represents a robust instrumental advancement, providing the community with a new route to build 2D THz spectrometers capable of achieving high electric fields for exploring complex dynamics in condensed matter.

II. SETUP OF THE 2D THZ SPECTROSCOPY

The schematic of the 2D THz spectroscopy platform is depicted in Fig. 1(a), comprising three key components: (i) dual high-intensity THz beam generation using tilted-pulse-front technique in separate $LiNbO_3$ crystals, (ii) spatiotemporal manipulation of THz beams, and (iii) nonlinear THz signal detection using electro-optical sampling (EOS) with a data acquisition card. We proceed to

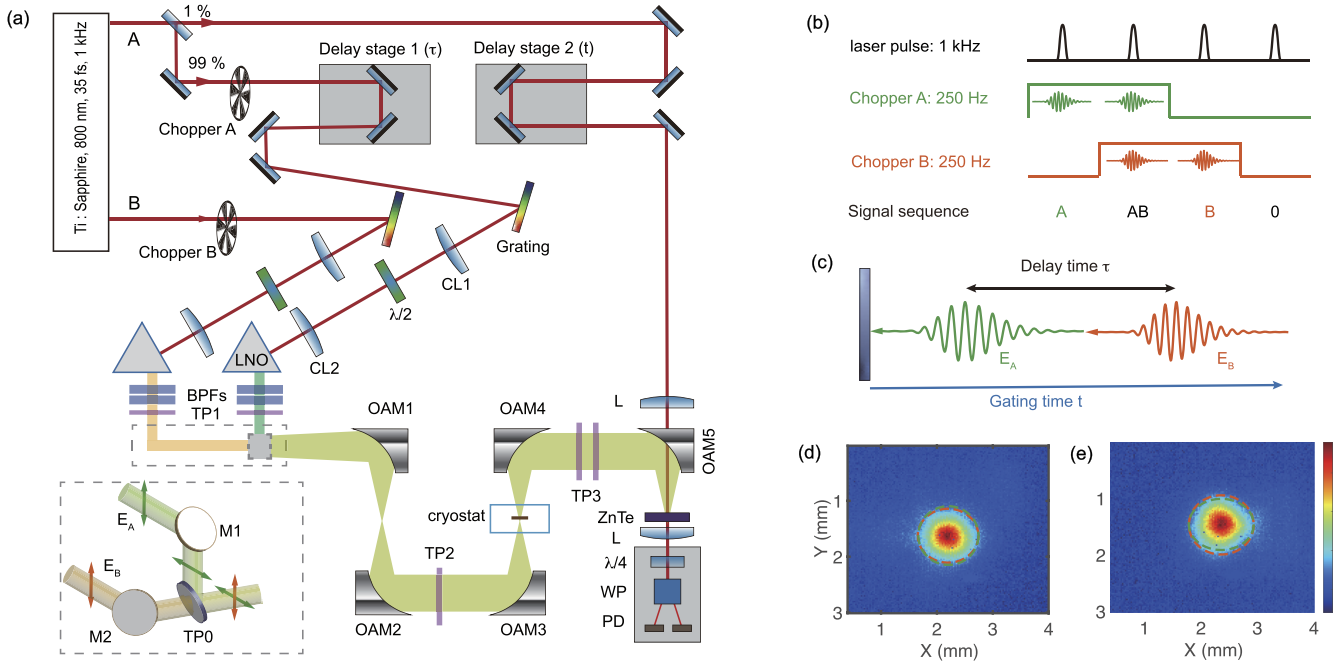

FIG. 1. (a) Schematic of the 2D THz spectroscopy platform with dual-crystal configuration. LNO: $LiNbO_3$ crystal; L: lenses; M: mirror; CL: cylindrical lenses; OAM: off-axis parabolic mirror; TP: THz polarizer; BPF: band-pass filter. The dashed section delineates the dual-beam combiner, comprising a reflective mirror and periscope assembly with orthogonally aligned mirror and THz polarizer (90° relative orientation). (b) Differential chopping detection scheme and THz transmission geometry. (c) Timing sequence of the two-pulse excitation in 2D THz spectroscopy. (d) and (e) THz beam profiles at sample and EOS detection positions, respectively, with dashed lines showing Gaussian fits to the overlapped dual-beam spots.

delineate the design specifications and the experimental implementation of the three constituent components in Secs. II A–II C.

A. Dual intense THz pulse generation

Two-dimensional terahertz spectroscopy requires two intense THz pulses with the electric field strong enough to induce nonlinear responses in the material. These pulses can be generated via optical rectification in nonlinear crystals such as $LiNbO_3$, utilizing either a single- or dual-crystal configuration. The former scheme employs two nearly collinear near-infrared pump beams incident on a single crystal, leading to the spatial overlap of the generated THz waves, which share identical polarization states.[43] This configuration restricts the subsequently independent manipulation of the two THz fields. On the other hand, the combination of two THz beams generated from dual-$LiNbO_3$ crystals usually utilizes a broadband THz polarizer oriented at 45° relative to the polarization direction of the THz pulses, where one polarized THz beam is transmitted while the other is reflected. However, this approach inherently reduces THz electric field strength by a factor of 0.7 and introduces challenges in achieving precise spatial overlap of the two THz beams at both the sample and EOS positions.

Here, we employ a dual-$LiNbO_3$ configuration and propose a novel method for THz beam combination that minimizes field strength loss while maintaining the versatile manipulation of THz pulses. As shown in Fig. 1(a), a Ti:sapphire amplified laser system with 800-nm center wavelength, 35-fs pulse duration, and 1-kHz repetition rate serves as the pump source. The amplifier has two independent compressor modules and delivers dual spatially separated outputs, denoted as beam A and beam B. Note that beam A, after the delay stage, is elevated by 5 cm relative to beam B through a standard periscope configuration incorporating two reflective mirrors. Two independent THz beams are generated via tilted-pulse-front optical rectification in MgO-doped $LiNbO_3$ crystal (CTL Photonics), where the MgO doping increases the damage threshold and mitigates the photo-refraction effect.[60] The crystal is cut at a prism angle of $\theta_{LN} = 62°$ to fulfill the velocity-matching condition given by $v_p^{gr} \cos\theta_{LN} = v_{THz}^{p}$, where v_p^{gr} is the group velocity of the pump laser and v_{THz}^{p} is the phase velocity of the THz wave within the crystal.[19] Initially, the pump beams A and B are individually directed onto gold-coated blazed gratings with groove densities of 1500 and 1700 lines/mm, respectively. These gratings introduce a pulse-front tilt through the $m = -1$ diffraction order with diffraction angle θ_d. After the grating, a $4f$ imaging system comprising two cylindrical lenses (f_1 = 100 mm, f_2 = 60 mm) relays the pump beams onto the crystal while maintaining a horizontal magnification factor $\beta_1 = 0.6$. A half-wave plate placed between the lenses rotates the polarization of the diffracted beam from horizontal to vertical, ensuring optimal THz generation efficiencies in the crystals.[19] The tilted angle γ of the pulse front is given by

$$\tan\gamma = \frac{m\lambda_0 p}{n_p^{gr}\beta_1 \cos\theta_d}, \tag{1}$$

where λ_0 is the central wavelength of the pump pulse, p is the groove density of the grating, and n_p^{gr} is the group refractive index of $LiNbO_3$ crystal at the pump pulse wavelength. The tilted angle γ must match the crystal prism angle for optimal THz generation.

TABLE I. Experimental configurations of dual THz pulse generation.

	Beam A	Beam B
$p\ (l/mm)$	1500	1700
$\theta_i\ (°)$	20.4	31.9
$\theta_d\ (°)$	58.2	56.3
$E_{NIR}\ (mJ)$	2.5	2.9
$E_{THz}\ (\mu J)$	9.1	10.5
$d_{THz}\ (mm)$	1.1	1
$E_{THz}\ (kV/cm)$ $(E_A \perp E_B)$	560	730
$E_{THz}\ (kV/cm)$ $(E_A \parallel E_B)$	390	510

The specific parameters in our instrument are summarized in Table I, where E_{NIR} is the pumping energy before the grating, and E_{THz} is the THz pulse energy measured by a commercial thermopile detector (Ophir 3A-P-THz) directly after the crystal. An optical-THz conversion efficiency of ~0.36% is achieved for both grating configurations.

B. THz beams manipulation

The generated THz waves (E_A and E_B), both initially polarized along the vertical direction, must be precisely aligned and focused collinearly to achieve optimal spatial overlap at both the sample and EOS positions. The key component of our 2D THz platform, enabling the polarization rotation and spatial recombination of the two THz beams, is a customized periscope assembly. It comprises a gold-coated reflective mirror (M1) cascaded with a high-extinction-ratio wire-grid THz polarizer (TP0) in a 90° rotated periscope configuration. The THz polarizer is oriented to transmit THz beams with vertical polarization while reflecting those with horizontal polarization. After reflecting off M1, E_A propagates vertically, followed by a subsequent reflection that turns the beam 90° to a horizontal direction. As indicated in the inset of Fig. 1(a), this process effectively rotates the polarization of E_A from vertical to horizontal. E_B is redirected by a mirror (M2) without altering its polarization state, thereby transmitting through TP0. Consequently, the combined dual THz beams exhibit orthogonal polarization states while preserving their individual electric field strength. Furthermore, the dual-reflector configuration for E_A enables precise spatial overlap of the two THz beams.

After the combination, the THz beams are carefully aligned and focused using a set of off-axis parabolic mirrors (OAMs), each with a diameter and effective focal length of 2 in. Due to the slight divergence of the THz radiation emitted from the $LiNbO_3$, the first OAM with a 2-in. diameter is employed to efficiently collect the THz beams. Following the initial focusing, the combined dual THz beams are collimated using OAM2 and subsequently refocused onto the sample position by OAM3. The overall energy transfer efficiency of the three OAMs was measured to be 60% for THz beam A and 52% for THz beam B. The THz pulses transmitted through the sample are re-imaged to the EOS position using a second pair of OAMs (OAM4 and OAM5). The specific focal lengths of OAMs are selected to achieve a tight focus at the sample plane, while also providing sufficient working distance for sample access and cryostat

integration. A continuous-flow liquid helium cryostat, equipped with two TPX windows, is mounted on an XYZ stage, allowing for accurate positioning of the sample at the THz focal point.

C. 2D THz signal detection

2D THz spectroscopy measures the nonlinear response arising from the interaction between the two intense THz pulses with a variable time delay.[61] To isolate the nonlinear signal, two mechanical choppers, synchronized to the laser repetition rate of 1 kHz, modulate beams A and B at a frequency of 250 Hz with a phase shift of $\pi/2$. As shown in a typical time sequence in Fig. 1(b), four distinct states of the probe pulses can be realized: I_A (pulse A), I_{AB} (pulse A + pulse B), I_B (pulse B), and I_0 (background noise). The signal sequences detected by EOS are sent to a data acquisition card following amplification by a voltage pre-amplifier. The THz electric field are record as $E_A = I_A - I_0$, $E_B = I_B - I_0$, and $E_{AB} = I_{AB} - I_0$. Therefore, the nonlinear signal is given by

$$E_{NL}(t,\tau) = E_{AB}(t,\tau) - E_A(t,\tau) - E_B(t), \quad (2)$$

where τ represents the inter-pulse delay between E_A and E_B, and t corresponds to the temporal axis of the EOS detection, as indicated in Fig. 1(c). The signal E_{NL} captures all orders of nonlinear response arising from the interaction of the two THz pulses. By applying the 2D Fourier transform with respect to t and τ, the temporal signal $E_{NL}(t,\tau)$ is converted into its frequency domain counterpart, $E_{NL}(\omega_t,\omega_\tau)$. The resulting 2D frequency spectrum reveals distinct features corresponding to different nonlinear orders and interaction sequences. Remarkably, the nonlinear signals are distributed across the 2D frequency domain (ω_t, ω_τ), with their positions determined by the specific nonlinear processes involved.[61] This approach enables the identification and separation of various nonlinear interaction processes, providing a comprehensive understanding of the material's response to the dual THz excitations.

D. THz beams characterization

In 2D THz spectroscopy, the strong electric field and precise spatial overlap of the dual THz pulses are essential as they directly determine the extent and nature of the nonlinear effects, which can

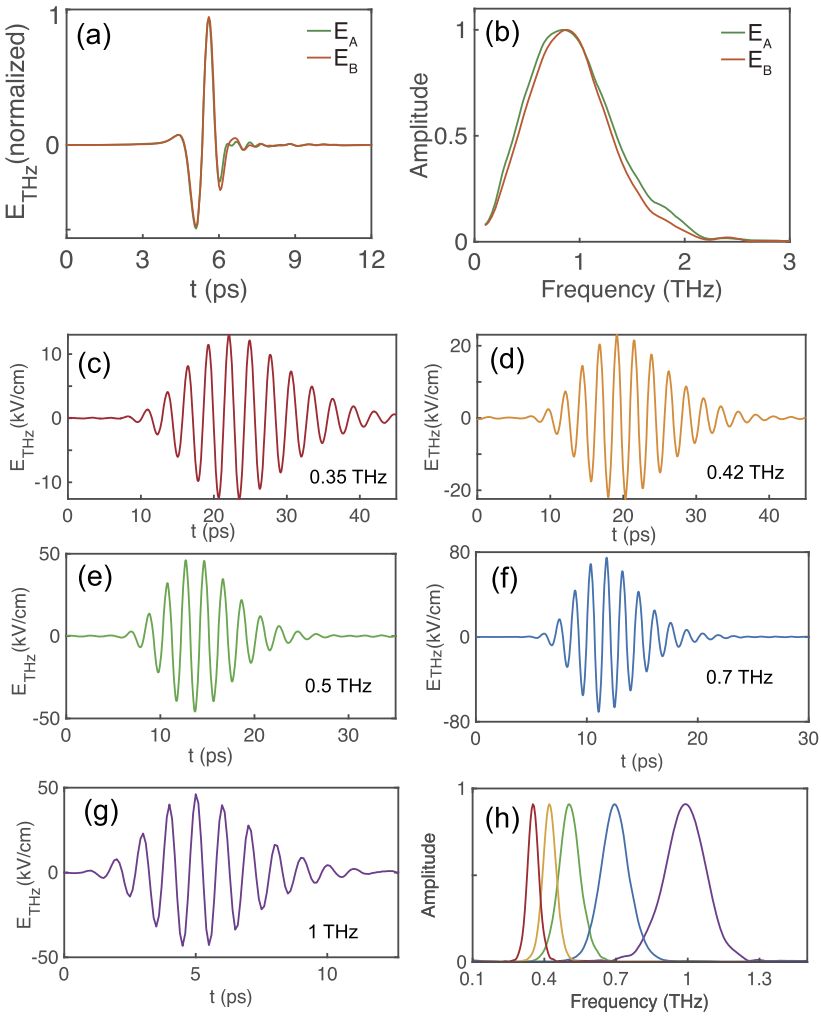

FIG. 2. Characterization of the THz beams. (a) Normalized temporal waveforms and (b) corresponding fast Fourier transform (FFT) spectra of E_A and E_B, measured via EOS using a 2-mm-thick ZnTe crystal. Both datasets were normalized for comparison. (c)–(g) Time-domain waveforms and (h) their respective FFT spectra of the multi-cycle THz pulses filtered at center frequencies of 0.35, 0.42, 0.5, 0.7, and 1 THz using two BPFs.

be explored in the experiments. The spatial overlap of the dual THz pulses at both the sample and EOS positions was examined using a commercial uncooled microbolometer camera (Swiss Terahertz S2x). As illustrated in Fig. 1(d), a radially symmetric THz beam spot with a $1/e^2$ diameter of ~1 mm was obtained at the sample position without the cryostat. The circles in the 2D diagram represent the Gaussian fitting results of the THz spot for E_A and E_B. Notably, similar results are observed at the EOS position, as shown in Fig. 1(e), demonstrating the excellent spatial overlap of the dual THz pulses throughout the beam path.

Figures 2(a) and 2(b) show the temporal waveforms and corresponding spectra of E_A and E_B measured via EOS using a 2-mm-thick ZnTe crystal. Following the procedure in Ref. 62, in the $E_A \perp E_B$ configuration, the peak electric field amplitudes of both THz pulses at the sample position were estimated as $E_A \sim 560$ kV/cm and $E_B \sim 730$ kV/cm, with a spectrum centered at 0.8 THz and extending to 2 THz.[62] For switching to $E_A \parallel E_B$ geometry, an additional THz polarizer (TP2) oriented at 45° relative to the horizontal direction is placed after OAM2. However, in such a geometry, the electric field of two THz beams is reduced to 70% of their peak fields. To prevent the detrimental nonlinear response from the ZnTe crystal, a pair of THz polarizers (TP3) was inserted before OAM5 to align the polarization and attenuate the intensity of the dual THz beams at the EOS sampling position.

To facilitate versatile manipulation of the dual intense THz pulses, the distance between the $LiNbO_3$ crystal and the first reflective mirror (M1 and M2) was set to ~10 cm. This spacing was specifically designed to accommodate individual optical components: two narrowband pass filters (BPFs) for selecting the desired narrowband pulses from the broadband THz radiation and a THz polarizer (TP1) for independent control of the polarization state and, hence, the field strengths of each combined beam. Figures 2(c)–2(g) show the time traces of the narrowband THz waves at frequencies of 0.35, 0.42, 0.5, 0.7, and 1 THz, respectively. The corresponding frequency-domain spectra are presented in Fig. 2(h). The ability to independently control the spectral, polarization, and intensity of each beam significantly enhances the system's versatility, enabling precise manipulation of terahertz waves for diverse applications.

III. RESULTS AND DISCUSSION

To demonstrate the capabilities of our instrument and facilitate the analysis of the complex 2D signals, we performed measurements on an *n*-type silicon wafer (Si, 0.6 mm thickness, 1×10^{15} cm^{-3} carrier density) using dual distinct multi-cycle THz pulses. Pulse E_A was centered at 0.5 THz with a peak electric field of 40 kV/cm, and pulse E_B was centered at 0.7 THz with a peak electric field of 80 kV/cm. These field strengths significantly exceed the threshold for nonlinear effects in semiconductors, where even a few kV/cm can induce measurable nonlinearities due to dominant free-carrier dynamics in the THz regime.[63–66] When both pulses illuminate the silicon, wave mixing processes occur,[67] generating new frequency components that are combinations of the incident 0.5 and 0.7 THz frequencies. Analysis of the frequency components and polarization dependence of the nonlinear signals allows for the elucidation of underlying mechanisms governing the observed nonlinear processes.

First, we measured the 2D nonlinear response from silicon with dual THz pulses in a parallel configuration. As mentioned above, an additional THz polarizer (TP2), oriented at 45° relative to the horizontal direction, was inserted after OAM2, which projects the dual orthogonal polarized THz pulses into a parallel configuration. Figure 3 illustrates the contour plots of $E_A(t,\tau)$, $E_B(t,\tau)$, $E_{AB}(t,\tau)$, and the nonlinear signal $E_{NL}(t,\tau)$, respectively. The exclusive presence of $E_{NL}(t,\tau)$ during the temporal overlap of both pulses confirms its nonlinear origin, arising from the interaction between the dual pulses rather than a response to either pulse individually.

To further analyze the nonlinear signal, the 2D spectrum of the nonlinear signal, $E_{NL}(\omega_t,\omega_\tau)$, was obtained by performing a 2D Fourier transform on $E_{NL}(t,\tau)$. As shown in Fig. 4(a), discrete spectral features are observed at specific frequencies. For

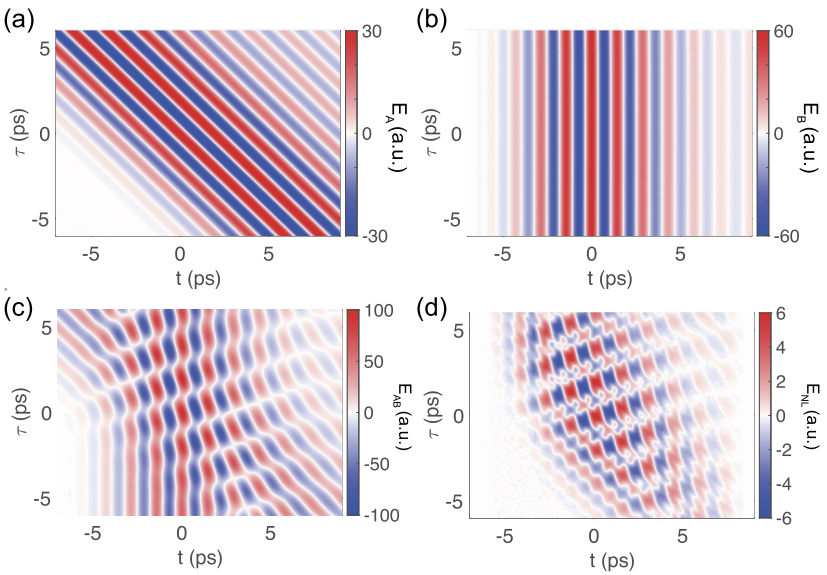

FIG. 3. 2D contour plots of (a) E_A, (b) E_B, (c) E_{AB}, and (d) E_{NL} as functions of probe delay t and relative delay τ between the dual THz pump pulses.

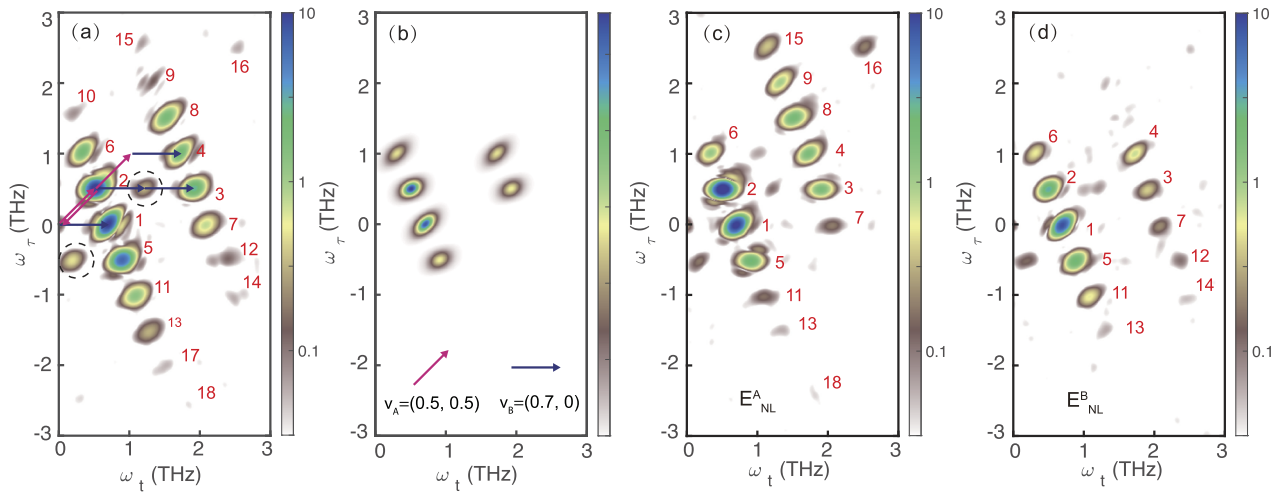

FIG. 4. (a) 2D spectra of $E_{NL}(\omega_t, \omega_\tau)$ measured with parallel-polarized E_A and E_B. (b) Simulated third-order nonlinear signals from Eq. (3). Arrows represent the frequency vectors of pulse A (ω_A, ω_A) and B $(\omega_B, 0)$. (c) and (d) 2D spectra of $E_{NL}(\omega_t, \omega_\tau)$ measured along the polarization directions of E_A and E_B, respectively, using cross-polarized THz pump beams.

centrosymmetric media such as silicon, third-order nonlinearity is the lowest non-vanishing term due to the absence of even-order effects.[65–67] For non-resonant interactions, the third-order polarization $P_3(t,\tau)$, which contains both pulse A and B, can be expressed as follows:

$$P_3(t,\tau) = \epsilon\chi_3[E_A^2(t,\tau)E_B(t) + E_A(t,\tau)E_B^2(t)], \tag{3}$$

where χ_3 is the third-order nonlinear susceptibility. The corresponding 2D Fourier spectrum of the simulated nonlinear response, using the above equation, is depicted in Fig. 4(b). The simulated results qualitatively reproduce the principal peak positions and general shapes observed experimentally, suggesting that the nonlinear signals (1–6) are dominated by third-order effects. However, the experimental data reveal additional features that are attributable to higher-order nonlinear processes, which are not captured in the simulation.

The complex nonlinear processes underlying the observed 2D signals can be visualized and understood using graphical methods, such as Feynman diagrams[59] and frequency vector analysis.[61] To facilitate the frequency vector analysis, we define two vectors, $\nu_A = (\omega_A, \omega_A)$ and $\nu_B = (\omega_B, 0)$, based on the wavefront of $(E_A(t,\tau))$ and $(E_B(t,0))$, as shown in Figs. 3(a) and 3(b). This representation allows us to depict interaction pathways as sequences of arrows, providing a clear and concise method for visualizing the evolution of the nonlinear signals. For example, as illustrated in Fig. 4(a), signal 1, located at $(\omega_B, 0)$, arises from the interaction sequence $\nu_A - \nu_A + \nu_B$, which can be expressed as $(\omega_A - \omega_A + \omega_B, \omega_A - \omega_A + 0)$. Similarly, signal 3, positioned at $(\omega_A + 2\omega_B, \omega_A)$, results from the sum frequency process represented by the interaction sequence $\nu_A + 2\nu_B$. Signals 7 and 8 might initially be attributed to the third-harmonic generation (THG) of E_B and E_A, respectively. However, as we have discussed above, only the signal involving cross-interactions between both pulses is experimentally resolvable in 2D spectroscopy. Instead, signals 7 and 8 are identified as fifth-order nonlinear signals originating from six-wave mixing processes. Specifically, signal 7 can be interpreted as E_A perturbing the third harmonic generation of E_B. The vectorial analysis readily indicates that signals 1–6, 7–12, 13–16, and 17 originate from third-, fifth-, seventh-, and ninth-order nonlinear processes, respectively.

A weak but clearly identifiable signal (labeled as 18) associated with an 11th-order effect via the interaction sequence $6\nu_B - 5\nu_A$ is resolved in both Figs. 4(a) and 4(c). This finding contrasts with previous studies of high-order THz nonlinearities in silicon, which were limited to one-dimensional high-harmonic generation (e.g., 3ω, 5ω, and 7ω from a single intense THz pulse) and required the extreme field strengths available at large-scale free-electron laser facilities or cryogenic temperatures to enhance the signal.[64] Our instrument allows for the direct resolution of such high-order processes in a 2D THz spectrum, distinguishing multiple contributions of the same order, even in silicon with a low carrier density.[65] This result demonstrates the high sensitivity and signal-to-noise ratio of the instrument.

All observed signals, their assigned interaction pathways, and corresponding frequency coordinates are summarized in Table II. The second-order signals, marked by dashed circles in Fig. 4(a), are identified as artifacts arising from sum- and difference-frequency generation between THz pulses A and B within the ZnTe detection crystal. These artifacts are effectively suppressed when the two THz beams are cross-polarized, as shown in Figs. 4(c) and 4(d). Control experiments were performed to verify the linear operating regime of the ZnTe detection and to rule out instrumental artifacts (Supplementary Material, Secs. S1–S3). In addition, systematic field-dependence measurements of the nonlinear signals (Supplementary Material, Sec. S4) validate our order assignments. Some signals also exhibit clear deviations from the expected power-law behavior. We attribute these deviations to saturation effects in the high-field, non-perturbative regime, rather than to measurement artifacts.[68] The

TABLE II. Nonlinear optical processes contributing to 2D THz signals in silicon.

Signal (order)	Nonlinear process	Frequency space
1 (3rd)	$\vec{\nu}_A - \vec{\nu}_A + \vec{\nu}_B$	$(\omega_B, 0)$
2 (3rd)	$\vec{\nu}_B - \vec{\nu}_B + \vec{\nu}_A$	(ω_A, ω_A)
3 (3rd)	$\vec{\nu}_A + 2\vec{\nu}_B$	$(\omega_A + 2\omega_B, \omega_A)$
4 (3rd)	$2\vec{\nu}_A + \vec{\nu}_B$	$(2\omega_A + \omega_B, 2\omega_A)$
5 (3rd)	$2\vec{\nu}_B - \vec{\nu}_A$	$(2\omega_B - \omega_A, -\omega_A)$
6 (3rd)	$2\vec{\nu}_A - \vec{\nu}_B$	$(2\omega_A - \omega_B, 2\omega_A)$
7 (5th)	$\vec{\nu}_A - \vec{\nu}_A + 3\vec{\nu}_B$	$(3\omega_B, 0)$
8 (5th)	$\vec{\nu}_B - \vec{\nu}_B + 3\vec{\nu}_A$	$(3\omega_A, 3\omega_A)$
9 (5th)	$4\vec{\nu}_A - \vec{\nu}_B$	$(4\omega_A - \omega_B, 4\omega_A)$
10 (5th)	$3\vec{\nu}_A - 2\vec{\nu}_B$	$(3\omega_A - 2\omega_B, 3\omega_A)$
11 (5th)	$3\vec{\nu}_B - 2\vec{\nu}_A$	$(3\omega_B - 2\omega_A, -2\omega_A)$
12 (5th)	$4\vec{\nu}_B - \vec{\nu}_A$	$(4\omega_B - \omega_A, -\omega_A)$
13 (7th)	$4\vec{\nu}_B - 3\vec{\nu}_A$	$(4\omega_B - 3\omega_A, -3\omega_A)$
14 (7th)	$5\vec{\nu}_B - 2\vec{\nu}_A$	$(5\omega_B - 2\omega_A, -2\omega_A)$
15 (7th)	$5\vec{\nu}_A - 2\vec{\nu}_B$	$(5\omega_A - 2\omega_B, 5\omega_A)$
16 (7th)	$\vec{\nu}_B - \vec{\nu}_B + 5\vec{\nu}_A$	$(5\omega_A, 5\omega_A)$
17 (9th)	$5\vec{\nu}_B - 4\vec{\nu}_A$	$(5\omega_B - 4\omega_A, -4\omega_A)$
18 (11th)	$6\vec{\nu}_B - 5\vec{\nu}_A$	$(6\omega_B - 5\omega_A, -5\omega_A)$

capability to resolve such saturation dynamics provides a quantitative demonstration of the instrument's performance and highlights its capability for studying non-perturbative phenomena at high fields.

To further assess the performance of our setup and characterize the nature of the nonlinear processes in silicon, we conducted polarization-dependent measurements of the nonlinear response with $E_A \perp E_B$ geometry. Figures 4(c) and 4(d) present the resulting 2D spectra of the nonlinear signals, E^A_{NL} and E^B_{NL}, detected via EOS optimizing along the E_A and E_B polarization directions, respectively. Due to the higher intensity of E_B (80 kV/cm) relative to E_A (40 kV/cm), the nonlinear responses exhibit distinct polarization-dependent features. For the E^B_{NL} polarization, the signal 1 at $(\omega_B,0)$ dominates over the signal 2 (ω_A, ω_A) component, while E^A_{NL} shows enhanced (ω_A, ω_A) response despite the lower E_A intensity. Furthermore, signals at positive τ [8, 9, 15, and 16 in Fig. 4(c)] appear predominantly in E^A_{NL}, whereas the nonlinear signals [12 and 14 in Fig. 4(d)] at negative τ but positive t are observed exclusively along the E^B_{NL} direction. These polarization-dependent features directly reveal the tensorial nature of the nonlinear susceptibilities in silicon, where the polarization of the nonlinear signal correlates strongly with the dominant driving field components. The comprehensive polarization analysis enabled by our 2D THz spectroscopy system provides quantitative insight into the nonlinear response of silicon, demonstrating both the advanced capabilities of our instrumental configuration and contributing valuable information to the fundamental understanding of nonlinear THz phenomena in semiconductor materials.

IV. CONCLUSION

We have developed and characterized a two-dimensional THz spectroscopy platform with a high electric field and complete experimental flexibility. A periscope-based combiner enables efficient beam combination and precise overlap of the two THz beams. This platform provides independent control over the polarization, spectrum, and intensity of two intense THz pulses. We demonstrated the instrument's performance by observing nonlinear wave-mixing signals up to the 11th order in silicon at room temperature, which showed a strong polarization dependence. These results establish the platform as a powerful tool for investigating complex material properties and fundamental light–matter interactions at THz frequencies, with future applications spanning condensed matter physics, materials science, and THz photonics.

SUPPLEMENTARY MATERIAL

See the Supplementary Material for (i) verification of the linear response of the EOS detection in a 2-mm-thick ZnTe crystal, (ii) measurement of the 2D THz background spectrum in the absence of a silicon sample, and (iii) field-dependence of the nonlinear signal amplitudes.

ACKNOWLEDGMENTS

This work was supported by the National Key Research and Development Program of China (Grant Nos. 2024YFA1611300, 2022YFA1403901, and 2022YFA1602802) and the National Natural Science Foundation of China (Grant Nos. 12250008, 12488201, and U24A2016). This work was carried out at the Synergetic Extreme Condition User Facility (SECUF, https://cstr.cn/31123.02.SECUF).

AUTHOR DECLARATIONS

Conflict of Interest

The authors have no conflicts to disclose.

Author Contributions

X. B. Wang and L. Y. Shi contributed equally to this work.

X. B. Wang: Funding acquisition (equal); Methodology (equal); Supervision (equal); Writing – original draft (equal); Writing – review & editing (equal). **L. Y. Shi**: Methodology (equal); Writing – original draft (equal); Writing – review & editing (equal). **S. J. Zhang**: Methodology (supporting); Writing – review & editing (supporting). **J. Y. Yuan**: Methodology (supporting). **Y. T. Li**: Funding acquisition (supporting); Writing – review & editing (supporting). **J. L. Luo**: Funding acquisition (supporting); Writing – review & editing (supporting). **T. Dong**: Funding acquisition (equal); Methodology (equal); Supervision (equal); Writing – original draft (equal); Writing – review & editing (equal). **N. L. Wang**: Funding acquisition (equal); Supervision (equal); Writing – original draft (equal); Writing – review & editing (equal).

DATA AVAILABILITY

The data that support the findings of this study are available from the corresponding authors upon reasonable request.

REFERENCES

[1] J. Jeener, B. H. Meier, P. Bachmann, and R. R. Ernst, J. Chem. Phys. **71**, 4546 (1979).
[2] H. Li, B. Lomsadze, G. Moody, C. Smallwood, and S. Cundiff, *Optical Multidimensional Coherent Spectroscopy* (Oxford University Press, 2023).
[3] S. Mukamel, Annu. Rev. Phys. Chem. **51**, 691 (2000).
[4] C. J. Fecko, J. D. Eaves, J. J. Loparo, A. Tokmakoff, and P. L. Geissler, Science **301**, 1698 (2003).
[5] D. M. Jonas, Annu. Rev. Phys. Chem. **54**, 425 (2003).
[6] M. L. Cowan, B. D. Bruner, N. Huse, J. R. Dwyer, B. Chugh, E. T. J. Nibbering, T. Elsaesser, and R. J. D. Miller, Nature **434**, 199 (2005).
[7] T. Brixner, J. Stenger, H. M. Vaswani, M. Cho, R. E. Blankenship, and G. R. Fleming, Nature **434**, 625 (2005).
[8] C. Kolano, J. Helbing, M. Kozinski, W. Sander, and P. Hamm, Nature **444**, 469 (2006).
[9] E. Fresch, F. V. A. Camargo, Q. Shen, C. C. Bellora, T. Pullerits, G. S. Engel, G. Cerullo, and E. Collini, Nat. Rev. Methods Primers **3**, 84 (2023).
[10] T.-T. Chen, M. Du, Z. Yang, J. Yuen-Zhou, and W. Xiong, Science **378**, 790 (2022).
[11] H. A. Hafez, X. Chai, A. Ibrahim, S. Mondal, D. Férachou, X. Ropagnol, and T. Ozaki, J. Opt. **18**, 093004 (2016).
[12] Y. Zhang, K. Li, and H. Zhao, Front. Optoelectron. **14**, 4 (2020).
[13] A. Fisher, Y. Park, M. Lenz, A. Ody, R. Agustsson, T. Hodgetts, A. Murokh, and P. Musumeci, Nat. Photonics **16**, 441 (2022).
[14] J. Hebling, G. Almási, I. Z. Kozma, and J. Kuhl, Opt. Express **10**, 1161 (2002).
[15] F. Blanchard, L. Razzari, H. C. Bandulet, G. Sharma, R. Morandotti, J. C. Kieffer, T. Ozaki, M. Reid, H. F. Tiedje, H. K. Haugen, and F. A. Hegmann, Opt. Express **15**, 13212 (2007).
[16] A. Sell, A. Leitenstorfer, and R. Huber, Opt. Lett. **33**, 2767 (2008).
[17] J. Hebling, K.-L. Yeh, M. C. Hoffmann, B. Bartal, and K. A. Nelson, J. Opt. Soc. Am. B **25**, B6 (2008).
[18] J. A. Fülöp, L. Pálfalvi, G. Almási, and J. Hebling, Opt. Express **18**, 12311 (2010).
[19] H. Hirori, A. Doi, F. Blanchard, and K. Tanaka, Appl. Phys. Lett. **98**, 091106 (2011).
[20] F. Blanchard, G. Sharma, L. Razzari, X. Ropagnol, H.-C. Bandulet, F. Vidal, R. Morandotti, J.-C. Kieffer, T. Ozaki, H. Tiedje, H. Haugen, M. Reid, and F. Hegmann, IEEE J. Sel. Top. Quant. Electron. **17**, 5 (2011).
[21] B. Zhang, Z. Ma, J. Ma, X. Wu, C. Ouyang, D. Kong, T. Hong, X. Wang, P. Yang, L. Chen, Y. Li, and J. Zhang, Laser Photonics Rev. **15**, 2000295 (2021).
[22] W. Kuehn, K. Reimann, M. Woerner, T. Elsaesser, and R. Hey, J. Phys. Chem. B **115**, 5448 (2011).
[23] T. Kampfrath, A. Sell, G. Klatt, A. Pashkin, S. Mährlein, T. Dekorsy, M. Wolf, M. Fiebig, A. Leitenstorfer, and R. Huber, Nat. Photonics **5**, 31 (2011).
[24] F. Blanchard, D. Golde, F. H. Su, L. Razzari, G. Sharma, R. Morandotti, T. Ozaki, M. Reid, M. Kira, S. W. Koch, and F. A. Hegmann, Phys. Rev. Lett. **107**, 107401 (2011).
[25] M. Liu, H. Y. Hwang, H. Tao, A. C. Strikwerda, K. Fan, G. R. Keiser, A. J. Sternbach, K. G. West, S. Kittiwatanakul, J. Lu, S. A. Wolf, F. G. Omenetto, X. Zhang, K. A. Nelson, and R. D. Averitt, Nature **487**, 345 (2012).
[26] T. Kampfrath, K. Tanaka, and K. A. Nelson, Nat. Photonics **7**, 680 (2013).
[27] R. Matsunaga, Y. I. Hamada, K. Makise, Y. Uzawa, H. Terai, Z. Wang, and R. Shimano, Phys. Rev. Lett. **111**, 057002 (2013).
[28] R. Matsunaga, N. Tsuji, H. Fujita, A. Sugioka, K. Makise, Y. Uzawa, H. Terai, Z. Wang, H. Aoki, and R. Shimano, Science **345**, 1145 (2014).
[29] X. Li, T. Qiu, J. Zhang, E. Baldini, J. Lu, A. M. Rappe, and K. A. Nelson, Science **364**, 1079 (2019).
[30] T. Dong, S.-J. Zhang, and N.-L. Wang, Adv. Mater. **35**, 2110068 (2023).
[31] J. Yuan, L. Shi, L. Yue, B. Li, Z. Wang, S. Xu, T. Xu, Y. Wang, Z. Gan, F. Chen, Z. Lin, X. Wang, K. Jin, X. Wang, J. Luo, S. Zhang, Q. Wu, Q. Liu, T. Hu, R. Li, X. Zhou, D. Wu, T. Dong, and N. Wang, Sci. Adv. **10**, eadg9211 (2024).
[32] W. Kuehn, K. Reimann, M. Woerner, T. Elsaesser, R. Hey, and U. Schade, Phys. Rev. Lett. **107**, 067401 (2011).
[33] F. Junginger, B. Mayer, C. Schmidt, O. Schubert, S. Mährlein, A. Leitenstorfer, R. Huber, and A. Pashkin, Phys. Rev. Lett. **109**, 147403 (2012).
[34] T. Maag, A. Bayer, S. Baierl, M. Hohenleutner, T. Korn, C. Schüller, D. Schuh, D. Bougeard, C. Lange, R. Huber, M. Mootz, J. E. Sipe, S. Koch, and M. Kira, Nat. Phys. **12**, 119 (2015).
[35] C. Somma, G. Folpini, K. Reimann, M. Woerner, and T. Elsaesser, Phys. Rev. Lett. **116**, 177401 (2016).
[36] S. Houver, L. Huber, M. Savoini, E. Abreu, and S. L. Johnson, Opt. Express **27**, 10854 (2019).
[37] Z. Zhang, F. Y. Gao, Y.-C. Chien, Z.-J. Liu, J. B. Curtis, E. R. Sung, X. Ma, W. Ren, S. Cao, P. Narang, A. von Hoegen, E. Baldini, and K. A. Nelson, Nat. Phys. **20**, 788 (2024).
[38] Z. Zhang, F. Y. Gao, J. B. Curtis, Z.-J. Liu, Y.-C. Chien, A. von Hoegen, M. T. Wong, T. Kurihara, T. Suemoto, P. Narang, E. Baldini, and K. A. Nelson, Nat. Phys. **20**, 801 (2024).
[39] C. Huang, L. Luo, M. Mootz, J. Shang, P. Man, L. Su, I. E. Perakis, Y. X. Yao, A. Wu, and J. Wang, Nat. Commun. **15**, 3214 (2024).
[40] S. Pal, N. Strkalj, C.-J. Yang, M. C. Weber, M. Trassin, M. Woerner, and M. Fiebig, Phys. Rev. X **11**, 021023 (2021).
[41] H.-W. Lin, G. Mead, and G. A. Blake, Phys. Rev. Lett. **129**, 207401 (2022).
[42] T. Blank, K. Grishunin, K. Zvezdin, N. Hai, J. Wu, S.-H. Su, J.-C. Huang, A. Zvezdin, and A. Kimel, Phys. Rev. Lett. **131**, 026902 (2023).
[43] K. A. Grishunin, V. R. Bilyk, E. D. Mishina, A. V. Kimel, and E. A. Mashkovich, Rev. Sci. Instrum. **94**, 073005 (2023).
[44] E. A. Mashkovich, K. A. Grishunin, R. M. Dubrovin, A. K. Zvezdin, R. V. Pisarev, and A. V. Kimel, Science **374**, 1608 (2021).
[45] C. Huang, M. Mootz, L. Luo, I. E. Perakis, and J. Wang, Nat. Rev. Phys. (published online 2026).
[46] L. Luo, M. Mootz, J. H. Kang, C. Huang, K. Eom, J. W. Lee, C. Vaswani, Y. G. Collantes, E. E. Hellstrom, I. E. Perakis, C. B. Eom, and J. Wang, Nat. Phys. **19**, 201 (2022).
[47] K. Katsumi, J. Fiore, M. Udina, R. Romero, D. Barbalas, J. Jesudasan, P. Raychaudhuri, G. Seibold, L. Benfatto, and N. Armitage, Phys. Rev. Lett. **132**, 256903 (2024).
[48] A. Liu, D. Pavićević, M. H. Michael, A. G. Salvador, P. E. Dolgirev, M. Fechner, A. S. Disa, P. M. Lozano, Q. Li, G. D. Gu, E. Demler, and A. Cavalleri, Nat. Phys. **20**, 1751 (2024).
[49] S. Zhang, Z. Sun, Q. Liu, Z. Wang, Q. Wu, L. Yue, S. Xu, T. Hu, R. Li, X. Zhou, J. Yuan, G. Gu, T. Dong, and N. Wang, Natl. Sci. Rev. **10**, nwad163 (2023).
[50] N. Taherian, M. Först, A. Liu, M. Fechner, D. Pavicevic, A. von Hoegen, E. Rowe, Y. Liu, S. Nakata, B. Keimer, E. Demler, M. H. Michael, and A. Cavalleri, npj Quantum Mater. **10**, 54 (2025).
[51] J. Yuan, L. Shi, T. Xu, Y. Wang, Z. Gan, H. Wang, T. Wu, D. Wu, T. Dong, and N. Wang, Phys. Rev. Lett. **135**, 166002 (2025).
[52] C. Huang, M. Mootz, L. Luo, D. Cheng, A. Khatri, J.-M. Park, R. H. J. Kim, Y. Qiang, V. L. Quito, Y. Yao, P. P. Orth, I. E. Perakis, and J. Wang, Sci. Adv. **11**, eads8740 (2025).
[53] N. Yoshikawa, H. Suganuma, H. Matsuoka, Y. Tanaka, P. Hemme, M. Cazayous, Y. Gallais, M. Nakano, Y. Iwasa, and R. Shimano, Nat. Phys. **17**, 909 (2021).
[54] C. Vaswani, L.-L. Wang, D. H. Mudiyanselage, Q. Li, P. M. Lozano, G. D. Gu, D. Cheng, B. Song, L. Luo, R. H. J. Kim, C. Huang, Z. Liu, M. Mootz, I. E. Perakis, Y. Yao, K. M. Ho, and J. Wang, Phys. Rev. X **10**, 021013 (2020).
[55] Y. Murotani, N. Kanda, T. Fujimoto, T. Matsuda, M. Goyal, J. Yoshinobu, Y. Kobayashi, T. Oka, S. Stemmer, and R. Matsunaga, Phys. Rev. Lett. **131**, 096901 (2023).
[56] F. Mahmood, D. Chaudhuri, S. Gopalakrishnan, R. Nandkishore, and N. P. Armitage, Nat. Phys. **17**, 627 (2021).
[57] C.-J. Yang, J. Li, M. Fiebig, and S. Pal, Nat. Rev. Mater. **8**, 518 (2023).
[58] I. A. Finneran, R. Welsch, M. A. Allodi, T. F. Miller, and G. A. Blake, Proc. Natl. Acad. Sci. **113**, 6857 (2016).
[59] J. Lu, X. Li, Y. Zhang, H. Y. Hwang, B. K. Ofori-Okai, and K. A. Nelson, Top. Curr. Chem. **376**, 6 (2018).
[60] X.-J. Wu, J.-L. Ma, B.-L. Zhang, S.-S. Chai, Z.-J. Fang, C.-Y. Xia, D.-Y. Kong, J.-G. Wang, H. Liu, C.-Q. Zhu, X. Wang, C.-J. Ruan, and Y.-T. Li, Opt. Express **26**, 7107 (2018).

[61] W. Kuehn, K. Reimann, M. Woerner, and T. Elsaesser, J. Chem. Phys. **130**, 164503 (2009).
[62] X. B. Wang, H. Wang, J. Y. Yuan, X. Y. Zeng, L. Cheng, J. Qi, J. L. Luo, T. Dong, and N. L. Wang, Rev. Sci. Instrum. **95**, 103007 (2024).
[63] M. C. Hoffmann, J. Hebling, H. Y. Hwang, K.-L. Yeh, and K. A. Nelson, J. Opt. Soc. Am. B **26**, A29 (2009).
[64] F. Meng, F. Walla, S. Kovalev, J.-C. Deinert, I. Ilyakov, M. Chen, A. Ponomaryov, S. G. Pavlov, H.-W. Hübers, N. V. Abrosimov, C. Jungemann, H. G. Roskos, and M. D. Thomson, Phys. Rev. Res. **5**, 043141 (2023).
[65] A. Mayer and F. Keilmann, Phys. Rev. B **33**, 6962 (1986).
[66] M. Urban, C. Nieswand, M. R. Siegrist, and F. Keilmann, J. Appl. Phys. **77**, 981 (1995).
[67] N. Dessmann, N. H. Le, V. Eless, S. Chick, K. Saeedi, A. Perez-Delgado, S. G. Pavlov, A. F. G. van der Meer, K. L. Litvinenko, I. Galbraith, N. V. Abrosimov, H. Riemann, C. R. Pidgeon, G. Aeppli, B. Redlich, and B. N. Murdin, Light Sci. Appl. **10**, 71 (2021).
[68] H. A. Hafez, S. Kovalev, J.-C. Deinert, Z. Mics, B. Green, N. Awari, M. Chen, S. Germanskiy, U. Lehnert, J. Teichert, Z. Wang, K.-J. Tielrooij, Z. Liu, Z. Chen, A. Narita, K. Müllen, M. Bonn, M. Gensch, and D. Turchinovich, Nature **561**, 507 (2018).